Disclination lines in nematic liquid crystal between a structured photoalignment layer and a homeotropic alignment layer

I. Nys, B. Berteloot, J. Beeckman, K. Neyts

LCP group, ELIS Department, Ghent University, Technologiepark 126, 9052 Gent, Belgium

Corresponding author: Kristiaan.neyts@ugent.be

Abstract

Topological defects in nematic liquid crystals (NLCs) are an interesting material system to study both from a theoretical point of view and for applications in photonics, soft-robotics and colloidal assembly. By using a photo-aligned template at one or both confining substrates, different disclination interconnections in the bulk can be readily stabilized. We imposed a periodic defect grid of 1/2 and -1/2 defects at the surface with the help of photoalignment and combined this with a uniform homeotropic counter substrate. This alignment configuration was used to study the optical properties and the relative stability of different types of disclinations in detail. The arrays of disclination lines are investigated by polarizing optical microscopy for different orientations of the polarizers and for different applied voltages. A theoretical analysis is performed to understand the relative frequency of occurrence for distinct types of disclinations and numerical simulations are used to verify the difference in optical appearance. The unequal elastic constants for splay, twist and bend strongly influence both properties and make it possible to identify different types of disclination lines form their optical appearance.

Introduction

Liquid crystals (LCs) are well known for their use in electro-optical devices, where a light beam is modulated with the help of an often defect-free director configuration. LC however also serves as a versatile material system to create, manipulate and study topological defects [1-21]. Many different techniques exist to create disclination lines in nematic LC, in which the nematic order is reduced and the director is not defined. Isolated defect loops and ordered or non-ordered arrays or different types of defects can exist in (passive and active) LC systems [2,3,6-14,22-30]. This offers new possibilities for electro-optical applications (tunable diffraction gratings, bistable devices with new switching modes, etc.) [6-11,23-26], colloidal assembly [27-28], polymer templating [29], etc. Homeotropic anchoring in combination with negative dielectric anisotropy LC, leads to the creation of umbilical defects when a voltage is applied [30]. A tunable and reconfigurable 2D array of umbilical defects can be obtained by doping the LC with an ionic impurity and applying an AC voltage [24]. The same material system can also be used in combination with micropillar arrays to control the periodicity and symmetry of the array of topological defects [25,26]. If two substrates with planar degenerate anchoring are used, disclination lines tend to connect defects on opposing sites, leading to the Schlieren texture [30]. If on the other hand patterned azimuthal anchoring at one substrate is combined with uniform planar anchoring at the opposite substrate, twist disclinations can as well be created [7-11]. Also electron-beam alignment, atomic force measurement scribing or photoalignment has made it possible to inscribe defect points on a substrate, in which the alignment direction is discontinuous [5,6,22,23,31]. Such alignment defects at the surface act as the source of one or more disclination lines in the nematic LC, which continue until they reach another defect. Several groups have reported the occurrence of disclination lines between a limited number of

defects or in a grid of defects. By exploiting photoalignment with well-chosen patterns, it is also possible to stabilize disclination lines that form a closed loop [7,8,10] or that are continuing over a distance of over 100 μm [8,12]. In the past, the curvature and the trajectory of disclination lines has been monitored, topological properties of LC disclination in two and three dimension have been studied and the influence of the cell thickness on the LC defect configuration has been investigated [18-21]. An extended study of the relative stability and the optical appearance of different types of disclination lines under the polarization microscope is still desirable. Detailed analysis of the optical appearance for different orientations of the polarizers can give additional information about the disclination line and the director orientation in its vicinity.

In this work we use a periodic photo-alignment grid of defects at the surface to create a large number of disclination lines in the bulk with different properties. Different from previous work [5,6], instead of planar anchoring we use uniform homeotropic anchoring (without azimuthal preference) at the top surface. The bulkdisclination lines appear differently when observed with polarization optical microscopy and some types occur more frequently than others. This can be understood from energy considerations, as we demonstrate with a simplified theoretical model. The aim is to link the observed disclination lines to particular structures that can be simulated with numerical tools. In this way we want to obtain a more detailed description of disclination lines and their behavior.

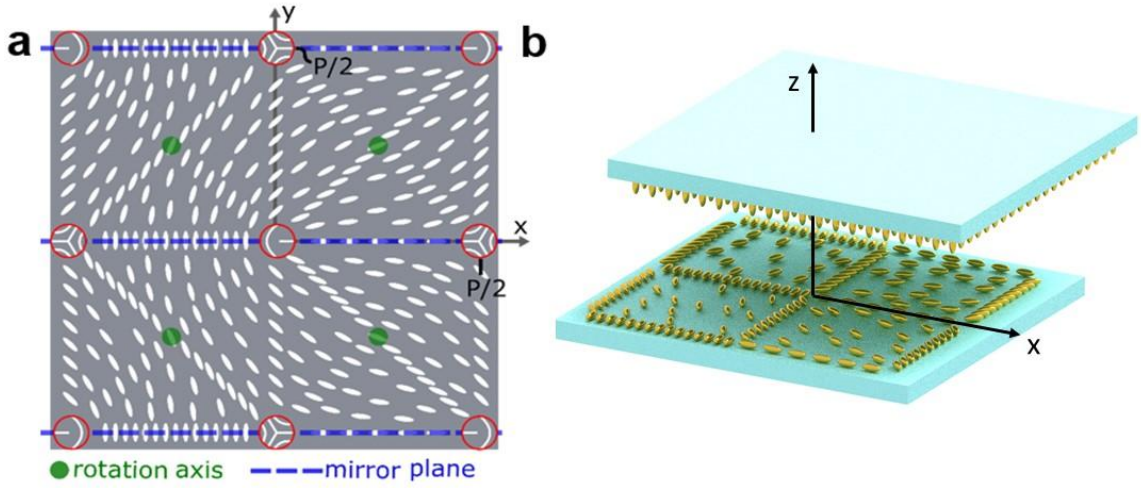

Figure 1. a Unit cell of the periodic photoalignment pattern on the bottom substrate. Each unit cell contains four defects: two with charge +1/2 and two with charge -1/2. The defects and the symmetry elements are indicated. **b** Structure of the unit cell: the top substrate has homeotropic alignment.

We will study the three-dimensional structures that are created when a nematic liquid crystal layer is sandwiched between a layer with patterned planar photoalignment and a layer with homeotropic alignment. For the alignment pattern we choose a periodic square grid of +1/2 and -1/2 defects with period P equal to 40 μm, with a continuous variation of the preferred director orientation between the defects, as illustrated in Fig. 1a. The alignment between the defects is defined by the angle φ between the x-axis and the preferred alignment direction (for defects $|x| < P/2$ and $|y| < P/2$) [5,22].:

$$\varphi(x,y) = \frac{1}{2}\arctan\frac{y.(P-2|y|)}{x.(P-2|x|)}$$

Near the bottom substrate the nematic LC director prefers to be oriented parallel to the substrate. In a defect point at the surface, the director orientation is not defined, and this leads to the creation of a ½ disclination line that continues into the bulk of the nematic LC. It is well known

that such ½ disclination lines cannot simply terminate in the bulk of the liquid crystal because of topological incompatibility. With the substrate condition provided by the experiment, the disclination lines always connect two topological defects of the alignment layer. However, this leaves many possibilities for interconnections to be formed when the LC is cooled down from the isotropic phase.

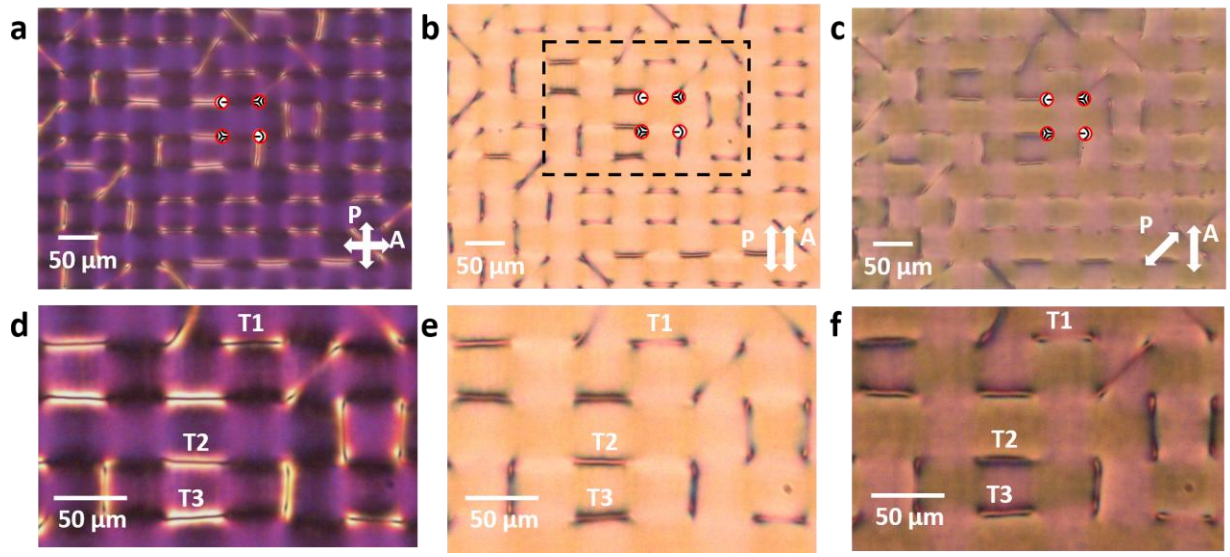

Figure 2. Polarization microscope images showing horizontal, vertical and diagonal disclination lines. The location, nature and orientation of four defects on the bottom substrate are indicated in red circles. **a** with crossed polarizers, **b** with parallel polarizers, **c** polarizers rotated over 45 degrees. The images **d**, **e** and **f** show a magnification of the region indicated in **b**. T1, T2 and T3 indicate three different types of horizontal discliantion lines as described in the text.

Results

Figure 2 shows the LC pattern observed with polarization optical microscopy after cooling down from the isotropic phase. The darkest areas in the image with crossed polarizers (Fig. 2a) are found along horizontal segments connecting the surface defects, regions where the director on the bottom substrate is oriented along x or along y (indicated by the blue dashed lines in Fig.1). The alignment at the top substrate is homeotropic, thus for these regions the director remains in

the xz plane or in the yz plane when going from the bottom to the top substrate and the transmission remains low between crossed polarizers (oriented along x and y respectively). The thickness of the device is about 5.5 μm and for a layer with hybrid alignment the retardation is about 0.55 μm. This leads to a transmission with minimum in the green and therefore the (non-dark) regions appear to be purple in the microscope image. The brightest purple regions are observed in the vertical sections where the azimuthal angle is +45° or -45° (with the director oriented along the bisector between the analyzer and the polarizer).

The disclination lines in the LC are easily identified in Figure 2a by linear sections with higher brightness (often in combination with a dark line in the center of the section). In Figure 2b, with parallel polarizers, the disclination lines are usually seen as regions with a darker appearance. As expected, the disclination lines are connecting nearest neighbors or second-nearest (diagonal) neighbors. It is striking that the disclination lines connecting nearest neighbors have different appearances. From Figures 2d and 2e we can recognize three types of horizontal (along x) disclination lines with length P/2, each with a different brightness. In Figure 2d one type appears relatively dark in the central part of the disclination line (indicated with T1), while the others consist of two bright lines surrounding the dark line (T2 and T3), with one type having brighter lines (T3) than the other. The last two (T2 and T3) can better be distinguished from microscopy images between parallel polarizers (Figure 2b and 2e), with one of them appearing brighter (T2) than the other one (T3). Also for the diagonal and vertical disclination lines different types are observed by polarization microscopy. This will be further discussed in the simulation and discussion section. In general, using different polarizer configurations can give rise to a more clear distinction between the different types of disclination lines.

In a region that is not near a disclination line, we expect the director to vary continuously from a well-defined planar orientation near the bottom substrate to the homeotropic orientation near the top substrate. Because the photo-alignment does not yield a pretilt and the homeotropic alignment layer is not rubbed, there are two options to realize this transition. For example for a director parallel to the x axis, either the +x side or the -x side can tilt towards +z direction at the top substrate. In the POM images of Fig. 2 the difference between these two cases cannot be distinguished. In order to discriminate between these two cases the device is first rotated over 45° around the z-axis and then tilted over 20°. The resulting images are shown in Fig. 3, with and without applied voltage.

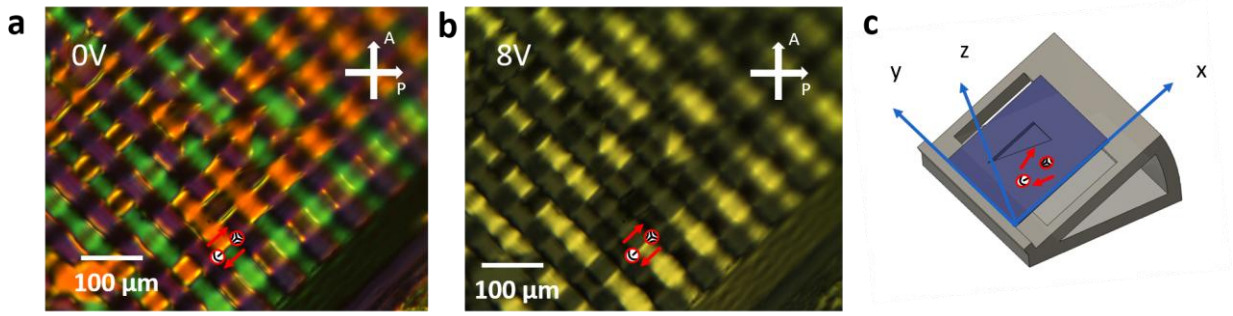

Figure 3. Polarization optical microscopy of the cell rotated over 45° and tilted over 20°. **a** without voltage applied, **b** with 8 V_{pp} peak to peak applied. **c** 3D image of the tilted measurement configuration. The nature of the defects is indicated in red circles. The director is indicated by a red arrow, with the head of the arrow pointing towards the +z direction. In the orange region (in **a**) or the dark region (in **b**) the director is tilted toward the +xz direction, leading to a smaller retardation when the device is tilted.

In Fig. 3a the disclination lines are still observed as bright stripes, but some regions have now obtained a green or orange color, although the alignment at the bottom substrate may be the same. To investigate which color corresponds to which type of tilt in the bulk, we have applied an ac voltage of $8V_{pp}$ (peak to peak) between the top and bottom electrode. The voltage aligns the director towards the z-axis and only in a small region near the bottom substrate the director

rotates towards the xy plane. For the red arrow in the dark region in Fig. 3b, the director rotates from +x to +z when moving along the z-axis. In this case the angle between the director and the propagation direction of the light is small, which leads to a small retardation between the eigenmodes, and a dark appearance. For the red arrow in the yellow region (Fig. 3b), the director rotates from -x to +z. In this case the light polarized in the xz plane experiences a much larger refractive index, because the director is at some point perpendicular to the light propagation direction. This leads to a larger retardation and hence a higher brightness. When the voltage is reduced to zero, we find that the orange region in Fig. 3a corresponds to the smaller retardation and the green region to the larger retardation. These regions are separated by the horizontal disclination lines or by regions with orientation along the y direction. From these considerations, we may conclude that the disclination lines that form a sharp border between a green and an orange region correspond to twist disclinations, with the director rotating around the y axis when encircling the disclination line. To confirm the detailed behavior it is important to compare the experimental results with simulations.

Numerical simulations

In this section we try to find stable 3D director orientations, that match the boundary conditions given in Figure 1. We assume strong anchoring on the bottom substrate (see Fig. 4g), according to the photoalignment pattern. The anchoring pattern (Fig. 4g) is translated with respect to the one in Fig. 1 in order to avoid the presence of surface defects at the edges of the simulation domain. In the simulations, the +1/2 defects are positions at (x, y) = (P/2, 3P/2), (3P/2, P/2) and the -1/2 defects are positions at (x,y) = (P/2,P/2), (3P/2, 3P/2). For the top substrate we use strong homeotropic anchoring without pretilt. At the boundaries with constant x or constant y, we assume periodic boundary conditions. The simulation is based on a minimization of the

Landau-de Gennes free energy, that is implemented in a finite element Q-tensor model (see methods section) [32-34].

The problem defined in this way has several solutions that are stable with respect to small deformations of the director. Each solution corresponds to a local minimum of the total free energy in the volume. The total free energy in one configuration may be higher than in another, but the transition from one to the other is not possible without a large deformation, such as creating a new disclination line to connect with a different defect. Accurately resolving the core of the disclinations and quantitatively describing the free energy in the different configurations is outside the scope of this work.

Figure 4 illustrates four different director configurations in the unit cell, each of them obtained after a minimization of the free energy after starting the simulation from different initial conditions. Many more solutions can be obtained as is explained in the discussion section. In each of the four solutions we observe two disclination lines that are parallel to each other when observed from the top. They can be horizontal (a,c), vertical (b) or diagonal (d). Each disclination line connects two defects on the bottom substrate, with either opposite charge (a,b,c) or the same charge (d). In the middle of the disclination line, the line is parallel to the substrates and roughly in the middle between the two substrates. Between the disclination line and the top substrate the director is more or less along the z-axis.

The optical simulations have been carried out with the open-source software Nemaktis developed by G. Poy. The simulation is based on a generalized beam propagation method for birefringent media [35]. Cauchy formulae are used for the refractive indices E7 and the spectrum of a CIE illuminant A is used to reproduce color images.

It is interesting to note that different types of disclination lines also appear differently in the simulated transmission images. This is clear for the disclination lines along the x axis in Fig. 4a and 4c. The two disclinations in Fig. 4a can be clearly distinguished from the ones in Fig. 4c. Additionally, a difference between the two disclination lines in Fig. 4c can be seen as well: when observed between parallel polarizers, the region around one of the disclination lines in Fig. 4c appears much darker than the other. It can be verified that these disclination lines are both of the wedge type, with the director rotating in a plane perpendicular to the disclination line, with the line for larger y having charge +1/2 and the line for lower y having charge -1/2.

We also carried out simulations with equal elastic constants of 12 pN, and this yields optical transmission images that are very similar for all horizontal disclination lines (see in Fig. 4e and 4f). We can conclude that the difference between the elastic constants for splay, twist and bend, with K_2 being the lowest, determines the optical appearance of the horizontal disclination lines.

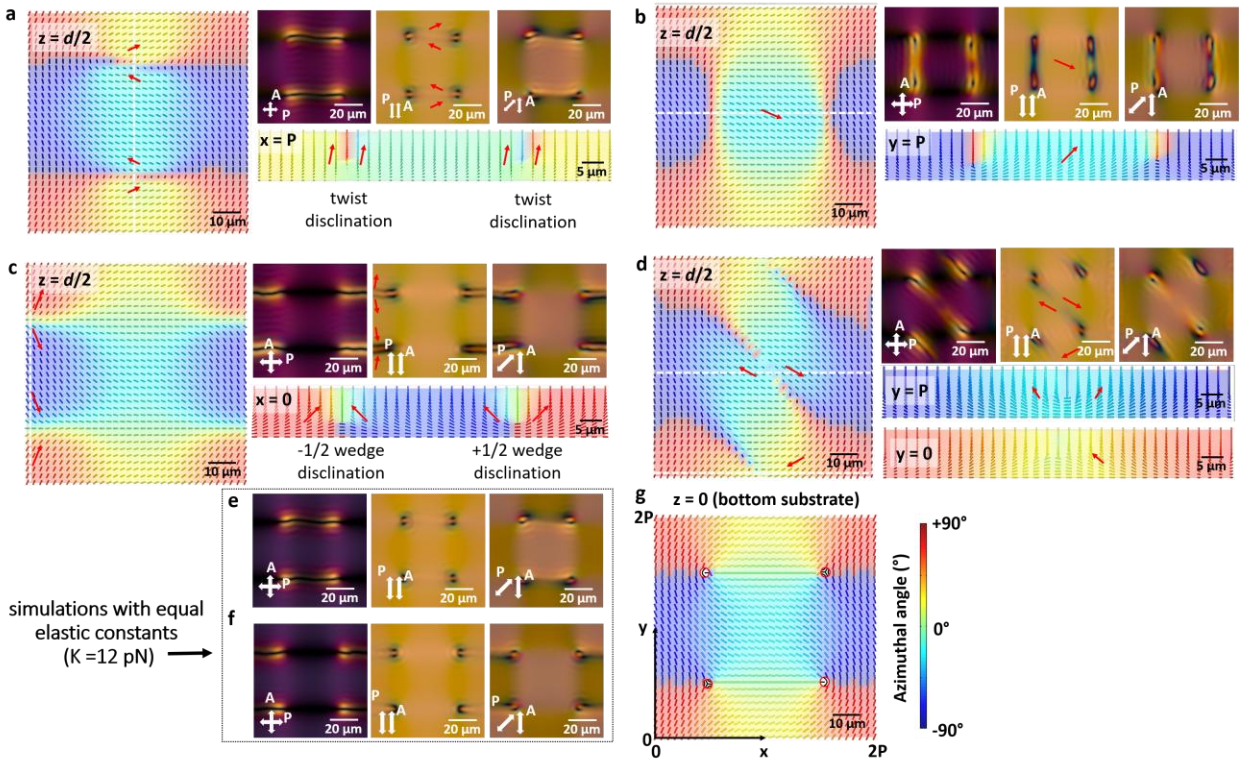

Figure 4. Simulation of stable director configurations with periodic boundary conditions. **a** horizontal disclination lines above regions with x-alignment, **b** vertical disclination lines, **c** horizontal disclination lines above regions with y alignment, **d** diagonal disclination lines Left: top view of the director in the midplane (the color represents the azimuthal angle of the director); bottom right: cross section of the director with constant x or y (indicated by the white dashed line in the left figure); top right: simulated transmission images; **e, f** simulated transmission images with equal elastic constants K=12 pN (for case a and c). **g** alignment configuration at the bottom substrate of the simulated unit cell. The red arrows shows the director, with the top of the arrow indicating the side with the highest z-coordinate.

Discussion

From a comparison between the polarization optical microscopy images (Fig. 2) and the simulated transmission patterns (Fig. 4), it can be seen that there is a good agreement. In particular we can recognize three types of horizontal disclination lines with different appearance in the microscope. The three types are indicated T1, T2 and T3 in Fig. 2 and the corresponding simulations are shown in Fig. 4(a) for T1 and Fig. 4(c) for T2 and T3 respectively. The three different types can be clearly distinguished by combining microscopy images for different

polarizer orientation. This agreement between simulations and experiments indicates that the director distribution in the devices is corresponding to the simulated three dimensional director patterns. Compared to our previous study of disclination lines in devices with planar alignment at the top surface [5], there are now different types of disclination lines, which we analyze from a theoretical point of view.

We can distinguish eight possible types of disclination lines between the +1/2 point defect in the center and the four nearest neighbors, as indicated in Fig.5. Four disclination lines are horizontal and four vertical. In these figures the disclination is indicated by a black line and the director orientation in the four quadrants and above the disclination line is indicated by a red arrow. As a reference, we assume that the director at the top surface is along the z-axis. Above the disclination line the director is roughly oriented towards the +z-axis.

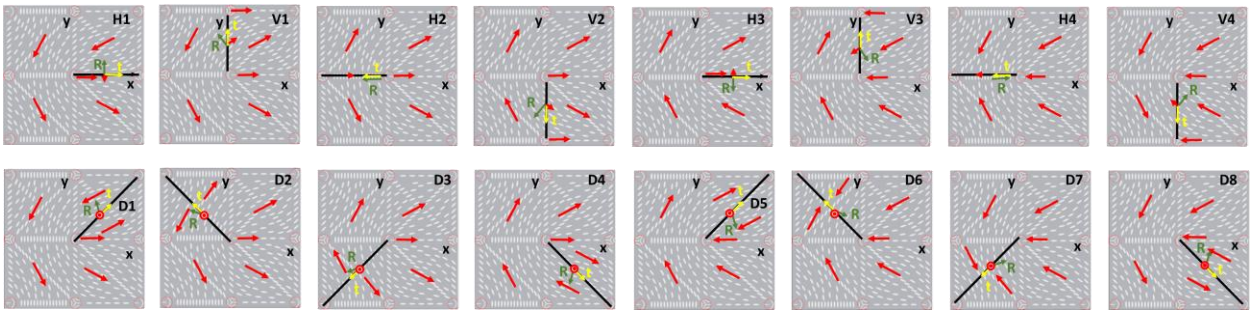

Figure 5. Schematic drawing of 16 possible disclination line connections for the +1/2 defect in the origin. The disclination lines are indicated with a black line, the red arrow indicates the director (the head of the arrow has the highest z-coordinate). The yellow arrow indicates the tangent vector t, the green arrow the rotation vector R. Top row: disclination lines connecting the nearest neighbors along x (H) or along y (V). Bottom row: disclination lines connecting with another +1/2 defect along a diagonal.

The director orientation in the neighborhood of the disclination line is determined by the photoalignment at the bottom substrate, the homeotrotropic alignment at the top substrate and the tilt angle in the neighboring quadrants. The rotation vector *R* can be used to describe the 180°

rotation of the director when encircling the disclination line. For reference we define the tangential vector *t* along the disclination line that starts in the defect in the origin. When encircling the disclination line according to the right hand rule with respect to the tangential vector *t*, the director describes roughly a half circle on the unit sphere according to the rotation vector *R*. The estimated orientation of the vectors *t* and *R* are indicated in Fig.5. In the +1/2 defect in the origin, the vector *R* points along +z. When leaving the defect along the disclination line, *R* rotates towards the xy plane until it becomes perpendicular to the photoalignment direction below the disclination line. The disclination line ends in the -1/2 defect, where the R vector is again parallel to the +z axis.

It is well know that the disclination line is of the twist type when *R* and *t* are perpendicular, and of the wedge type (without twist elastic energy) when *R* and *t* are parallel or antiparallel. For other angles between *R* and *t* the nature of the disclination line is mixed. Because the twist elastic constant is smaller than the splay and bend elastic constants, the rotation vector has the tendency to deviate away from the tangential direction. In addition it is clear that bending of the disclination line and variations of the rotation vector require additional energy.

The above considerations allow to understand how the rotation vector varies between the surface defects (*R* along +z) and the middle of the defect: tilted towards the xy plane, towards an azimuthal direction perpendicular to the photoalignment direction. We can also estimate the total elastic energy for the eight cases connecting nearest neighbors. The lines H1 and H3 (which are each other's mirror image with respect to the xz plane, Fig. 5) have the lowest elastic energy because the disclination is of the twist type. The four vertical disclination lines have somewhat higher energy, because the disclination line is of the mixed type. Finally case H2 and H4 have the highest elastic energy, because the disclination line is of the wedge type. The +1/2

disclination in the center of Fig. 5 can be rotated over 180° with respect to the z-axis. In this case eight equivalent disclination lines can be found, which are simply rotated over 180° compared to the disclination lines in Fig. 5. To specify their nature, we refer to them with an additional letter R, for example H1R for T1; H2R for T2 while we use H4 for T3 in Fig. 2. In total there are therefore sixteen different disclination lines connecting nearest neighbors.

For the diagonal disclination lines, that connect surface defects with the same charge, a similar analysis can be made. We can distinguish sixteen different diagonals, eight for the +1/2 and eight for the -1/2 disclinations. The eight different diagonals that connect +1/2 surface defects are schematically shown in Fig. 5 (bottom row) and are labeled D1 to D8. The diagonals can be connected in 4 different directions and for each direction there are two possibilities, in which the director has the opposite tilt angle with respect to the xy plane. Disclination lines that connect -1/2 defects can be classified in a similar way, with labels D1- to D8-.

In total, for the periodic alignment pattern on the bottom substrate of Fig. 1 and homeotropic alignment at the top substrate, we can distinguish thirty two different connections between nearest neighbors or second-nearest (diagonal) neighbors. Some of these disclination lines are each other's mirror image, and some are identical after a rotation over 180 degrees. Taking the symmetries into account, we find thirteen different kinds of disclination lines, each of them with a particular elastic energy. The classification of the different lines is shown in the table in Fig. 6a. We make a rough estimate of the elastic energy in each disclination line, taking into account the length of the disclination line (20 μm for connections between nearest neighbors, 28 μm for the diagonals) and the angle β between the tangential vector and the rotation vector, using the equation below (see supplementary information S1). In this formula, the energy related to biaxiality and the reduction of the order parameter in the core of the disclination is neglected.

$$F_{discl} = \frac{\pi}{16} \ln \frac{r_{max}}{r_{core}} \left(K_{11} \left(1 + \cos^2 \beta\right) + 2K_{22} \sin^2 \beta + K_{33} \left(1 + \cos^2 \beta\right) \right)$$

Using the elastic energy constants for E7, r_{max}= 2 µm, r_{min} = 10 nm and the appropriate values for β, we obtain the energy of the disclination lines, as shown in the table in Fig. 6. Fig. 6b illustrates the classification for the disclination lines, for a selection of Fig. 2b. The red arrows indicate the director, with the head of the arrow having the higher z-coordinate. From Fig. 2 and Fig. S2 (supplementary information) it can be seen that some types occur more frequently than others, and there is an inverse correlation with the elastic energy (estimated in Fig. 6a). For example type H1/H3/H1R/H3R is the most abundant type (20 times in Fig. 2b with the lowest estimated energy 0.86 fJ), while there are only three disclination lines with the highest energy (D3 and two times D7- in Fig. 2b, with estimated energy 1.59 fJ).

a

character	example	xz mirrored	rotated	β (°)	energy (fJ)
horizontal twist	H1	H3	H1R, H3R	90	0,86
horizontal wedge +1/2	H2		H2R	0	1,17
horizontal wedge -1/2	H4		H4R	180	1,17
vertical	V1	V2	V1R, V2R	45	1,02
	V3	V4	V3R, V4R	135	1,02
diagonal+	D1	D4		67,5	1,28
	D2	D3		22,5	1,59
	D5	D8		112,5	1,28
	D6	D7		157,5	1,59
diagonal-	D1-	D4-		67,5	1,28
	D2-	D3-		22,5	1,59
	D5-	D8-		112,5	1,28
	D6-	D7-		157,5	1,59

b

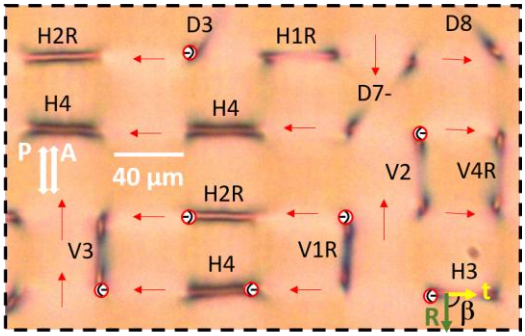

Figure 6. Classification of the 32 disclination lines. **a** The table distinguishes the 13 different types, with each type having mirrored and/or rotated representations. Also listed is the angle β between the disclination line and the rotation vector and the estimated elastic energy. **b** Selected part of Fig.2b showing different disclination lines, each of them with their classification name. Some of the +1/2 defects are indicated by a symbol and some directors are indicated by a red arrow. For the H3 disclination the tangential vector t, the rotation vector R and the angle β between them are shown.

Conclusion

We have demonstrated that by combining a photoalignment pattern with defects at the bottom substrate and homeotropic alignment at the top substrate, disclination lines of different types

appear in nematic LC. By comparing polarization optical microscopy images with numerical simulations of the transmission near disclination lines, different types of disclination lines could be identified. From a theoretical analysis thirteen different types, with a specific free energy, could be identified: five types connect nearest neighbor defects and eight types connect defects with the same charge across the diagonal. For every defect on the surface, there are sixteen different ways to connect with another defect (nearest or second-nearest) through a disclination line. A negative correlation is found between the frequency of occurrence of a disclination line and its total elastic energy. By using polarization microscopy, different types of disclination lines can be optically distinguished. We have shown that the different magnitude of the elastic constants for splay, twist and bend determines not only the relative frequency of occurrence of the different disclination lines, but also allows to identify the different disclination lines from their optical appearance.

The connection between defects on the surface with disclination lines is stable with respect to applied voltages or temperature, and could be used as a way to store information. The dimensions of the defect grid could be much further reduced and the different states can be read using optical transmission. For a periodic grid of disclination lines, interesting diffraction properties can be obtained. Switching between different states may be induced by strong voltage pulses inducing flow or by mechanical pressure.

Methods

Device Design

To fabricate the device, two glass substrates are cleaned and treated with UV-Ozone (15 min. at 90°C). Both substrates are one inch by one inch and have an ITO coating that is used as a

transparent electrode. The bottom substrate is spin-coated with a photoalignment layer that consists out of 0.2 wt% Brilliant Yellow in dimethylformamide (both bought from Sigma-Aldrich, spin speed 3000 rpm for 30 s). After spin-coating, the sample is placed on a hot plate (5 minutes at 90 °C). To achieve the desired periodic pattern, the projection of a spatial light modulator (SLM) is used. [7] The SLM (Holoeye Pluto-2, 1920x1080 pixels, 8 μm pitch) is illuminated by a blue laser (Cobolt Twist, 457 nm, 200 mW) with circular polarization. The image displayed by the SLM defines different phase retardations. Using a quarter-wave plate, these phase retardations are converted into different rotations of linear polarization. The LC director will orient perpendicular to the orientation of linear polarization. A lens is used to scale down the image of the SLM approximately 11.6 times. The period in the pattern of the scaled down image is set to 40 μm.

The top substrate is spin-coated with a homeotropic alignment layer (SE4811, Nissan Chemical Industries, spin speed 2500 rpm for 15 s). After the spin coating, the substrate is prebaked on a hotplate (90 °C) for two minutes. The layer is then cured for one hour in an oven at 180 °C. Once the alignment layers are prepared, the substrates are glued together (NOA 68). To define the cell thickness, spacers with a diameter of 5.5 μm are mixed in the glue. After the glue is cured, the cell is placed on a hot plate (80 °C) and filled with E7.

Numerical Simulations

To simulate the director configuration, the Landau-de Gennes free energy is minimized with the help of a finite element method. The LC is represented by the Q-tensor, a symmetric rand two tensor that describes the molecular orientation and the LC order. The total free energy is the sum of elastic distortion energy, thermotropic (or Landau) energy, electrical energy and surface energy[32-34]. Each energy term can be expressed as a function of Q and its spatial derivatives. The material parameters for E7 are used (K_{11} = 11.1 pN, K_{22} = 6.5 pN, K_{33} = 17.1 pN, ε_{perp} = 5.2,

ε_{para} = 19) together with the Landau coefficients A = -174 N/m^2, B = -2120 N/m^2, C = 1740 N/m^2). At the top and bottom boundaries we assume strong anchoring with 90° pretilt for the homeotropic top substrate and zero pretilt for the photo-aligned bottom substrate, with azimuthal anchoring defined by equation 1. Periodic boundary conditions are applied for the interfaces at $|x| = P/2$ and $|\mathbf{y}| = P/2$. The numerical solutions in the volume contain disclination lines and the mesh is sufficiently small to ensure the mobility of the disclination lines during the optimization process.

The optical simulations of the transmission (for different orientation of the polarizers) have been carried out with the open-source software Nemaktis developed by G. Poy. The simulation is based on a generalized beam propagation method for birefringent media [35]. Cauchy formulae are used for the refractive indices of E7 and the spectrum of a CIE illuminant A is used to reproduce color images. The incident light is linearly polarized, and after transmission through the LC layer the light passes through a second polarizer.

References

1. S. Zhou, S. V. Shiyanovskii, H.-S. Park, O. D. Lavrentovich, Fine structure of the topological defect cores studied for disclinations in lyotropic chromonic liquid crystals, Nature Communications, 8, 14974, 2017. DOI: 10.1038/ncomms14974

2. J. Binysh, Z. Kos, S. Copar, M. Ravnik, G. P. Alexander, Three-Dimensional Active Defect Loops, Physical Review Letters 124, 088001 (2020).

3. G. Duclos, R. Adkins, D. Banerjee, M.S.E. Peterson, M. Varghese, I. Kolvin, A. Baskaran, R. A. Pelcovits, T. R. Powers, A. Baskaran, F. Toschi, M. F. Hagan, S. J. Streichan, V. Vitelli, D. A. Beller, Z. Dogic, Topological structure and dynamics of three-dimensional active nematics. *Science* 2020, **367**(6482)**:** 1120-1124.

4. E. K. Omori, R. S. Zola, R. Teixeira de Souza, Stable disclination lines in nematic liquid crystals confined in thin films with periodic-planar surfaces: A Monte Carlo study, Journal of Molecular Liquids 342 (2021) 117538. DOI: 10.1016/j.molliq.2021.117538

5. I. Nys, B. Berteloot, J. Beeckman, K. Neyts, Nematic liquid crystal disclination lines driven by a photo-aligned defect grid, Advanced Optical Materials 2021, 2101626. DOI: 10.1002/adom.202101626

6. Y. Guo, M. Jiang, S. Afghah, C. Peng, R. L. B. Selinger, O. D. Lavrentovich, Q.-H. Wei, Photopatterned designer disclination networks in nematic liquid crystal, Advanced Optical Materials (2021), 2100181

7. B. Berteloot, I. Nys, G. Poy, J. Beeckman, K. Neyts, Ring-shaped liquid crystal structures through patterned planar photo-alignment. *Soft Matter* 2020, **16**(21)**:** 4999-5008.

8. I. Nys, Patterned surface alignment to create complex three-dimensional nematic and chiral nematic liquid crystal structures. *Liquid Crystals Today* 2020, **29**(4)**:** 65-83.

9. G.P. Crawford, J.N. Eakin, M.D. Radcliffe, A. Callan-Jones, R. A. Pelcovits, Liquid-crystal diffraction gratings using polarization holography alignment techniques. J Appl Phys. 2005;98:1231021.

10. K. Sunami, K. Imamura, T. Ouchi, H. Yoshida, M. Ozaki, Shape control of surface-stabilized disclination loops in nematic liquid crystals. Phys Rev E. 2017;97(2):020701.

11. Nys I, Berteloot B, Poy G. Surface stabilized topological solitons in nematic liquid crystals. Crystals. 2020;10(9):840.

12. M. F. Wang, Y. N. Li, H. Yokoyama, Artificial web of disclination lines in nematic liquid crystals. *Nat Commun* 2017, **8**.

13. K. Harth, R. Stannarius, Topological Point Defects of Liquid Crystals in Quasi-Two-Dimensional Geometries. *Front Phys-Lausanne* 2020, **8**.

14. S. Copar, S. Zumer, Quaternions and hybrid nematic disclinations. *P Roy Soc a-Math Phy* 2013, **469**(2156).

15. C. Long, X. Tang, R. L. B. Selinger, J. V. Selinger, Geometry and mechanics of disclination lines in 3D nematic liquid crystals. *Soft Matter* 2021(17)**:** 2265-2278. DOI: 10.1039/D0SM01899F

16. I.I. Smalyukh, B.L. Senyuk, S.V. Shiyanovskii, O.D. Lavrentovich, A.N. Kuzmin, A.V. Kachynski, P. N. Prasad, Optical trapping, manipulation, and 3D imaging of disclinations in liquid crystals and measurement of their line tension. *Mol Cryst Liq Cryst* 2006, **450:** 279-295.

17. E.C. Gartland, Forces and variational compatibility for equilibrium liquid crystal director models with coupled electric fields. *Continuum Mech Therm* 2020, **32**(6)**:** 1559-1593.

18. A.L. Susser, S. Harkai, S. Kralj, C. Rosenblatt, Transition from escaped to decomposed nematic defects, and vice versa. *Soft Matter* 2020, **16**(20), 4814-4822. DOI: 10.1039/D0SM00218F

19. M. Ambrozic, S. Kralj, Thickness induced line-defect reconfigurations in thin nematic cell. Advances in Condensed Matter Physics 2019, 4256526 1-7. DOI: 10.1155/2019/4256526

20. S. Afghah, R.L.B. Selinger, J.V. Selinger, Visualising the crossover between 3D and 2D topological defects in nematic liquid crystals. *Liq. Cryst.* 2018, **45**, 2022. DOI: 10.1080/02678292.2018.1494857

21. A.J. Ferris, S. Afghah, R.L.B. Selinger, J.V. Selinger, C. Rosenblatt, Electric field-induced crossover from 3D to 2D topological defects in a nematic liquid crystal: experimental verification. *Soft Matter* 2020, **16**(3), 642-650. DOI: 10.1039/c9sm01733j

22. B.S. Murray, R.A. Pelcovits, C. Rosenblatt, Creating arbitrary arrays of two-dimensional topological defects. *Phys Rev E* 2014, **90**(5) 052501. DOI: 10.1103/PhysRevE.90.052501

23. S. Harkai, B. S. Murray, C. Rosenblatt, S. Kralj, Phys. Rev. Research. 2020, 2, 013176 Electric field driven reconfigurable multistable topological defect patterns. DOI: 10.1103/PhysRevResearch.2.013176

24. Y. Sasaki, V. S. R. Jampani, C. Tanaka, N. Sakurai, S. Sakane, K. V. Le, F. Araoka, H. Orihara, Large-scale self-organization of reconfigurable topological defect networks in nematic liquid crystals, Nature Communications, 7, 13238, 2016. DOI: 10.1038/ncomms13238

25. M. Kim, F. Serra, Topological Defect Arrays in Nematic Liquid Crystals Assisted by Polymeric Pillar Arrays: Effect of the Geometry of Pillars. *Crystals* 2020, **10**(4).

26. M. Kim, F. Serra, Tunable Dynamic Topological Defect Pattern Formation in Nematic Liquid Crystals, Advanced Optical Materials 2020, 8, 1900991. DOI: 10.1002/adom.201900991

27. H. Yoshida, K. Asakura, J. Fukuda, M. Ozaki, Three-dimensional positioning and control of colloidal objects utilizing engineered liquid crystalline defect networks. *Nat Commun* 2015, **6,** 7180. DOI: 10.1038/ncomms8180.

28. J.B. Fleury, D. Pires, Y Galerne, Self-Connected 3D Architecture of Microwires. *Phys Rev Lett* 2009, **103**(26).

29. G. Babakhanova, T. Turiv, Y. Guo, M. Hendrikx, Q.-H. Wei, A. P.H.J. Schenning, D. J. Broer, O. D. Lavrentovich, Liquid crystal elastomer coatings with programmed response of surface profile, Nature Communications 2018, 9:456. DOI: 10.1038/s41467-018-02895-9

30. I. Dierking, O. Marshall, J. Wright. N. Bulleid, Annihilation dynamics of umbilical defects in nematic liquid crystals under applied electric fields, Physical Review E 71, 061709, 2005. DOI: 10.1103/PhysRevE.71.061709

31. I. Nys, J. Beeckman, K. Neyts, Surface-mediated alignment of long pitch chiral nematic liquid crystal structures, Advanced Optical Materials 6 (13), 1800070, 2018. DOI: 10.1002/adom.201800070

32. P.G. de Gennes, J. Prost, *The Physics of Liquid Crystals*. Clarendon Press, 1993.

33. R. James, E. Willman, F. A. Fernandez, S. E. Day, Finite-element modeling of liquid-crystal hydrodynamics with a variable degree of order. *Ieee T Electron Dev* 2006, **53**(7)**:** 1575-1582.

34. R. James, E. Willman, R. Ghannam, J. Beeckman, F.A. Fernández, Hydrodynamics of fringing-field induced defects in nematic liquid crystals. Journal of Applied Physics, (2021) (Accepted for Publication).

35. G. Poy, S. Zumer, Physics-based multistep beam propagation in inhomogeneous birefringent media. *Opt Express* 2020, **28**(16)**:** 24327-24342.

Supplementary Information

S1 Estimation of the energy in a disclination line, assuming three different elastic constants.

The elastic energy density by Oseen and Frank, as a function of the director L is given by:

$$F = \frac{1}{2}K_{11}\left(\nabla\cdot\bar{L}\right)^2 + \frac{1}{2}K_{22}\left(\bar{L}\cdot\nabla\times\bar{L}\right)^2 + \frac{1}{2}K_{33}\left(\bar{L}\times\nabla\times\bar{L}\right)^2$$

Working in cylinder coordinates (r,φ,z'), with the z' axis chosen along t (along the disclination line) and neglecting the z'-dependency in the variation of the director we obtain:

$$F = \frac{1}{2}K_{11}\left(\frac{1}{r}L_r + \frac{1}{r}\frac{\partial L_\varphi}{\partial\varphi}\right)^2 + \frac{1}{2}K_{22}\left(L_r\frac{1}{r}\frac{\partial L_{z'}}{\partial\varphi} + \frac{L_{z'}}{r}L_\varphi - \frac{L_{z'}}{r}\frac{\partial L_r}{\partial\varphi}\right)^2 + \frac{1}{2}K_{33}\left(\left(\frac{1}{r}L_\varphi L_\varphi - \frac{1}{r}L_\varphi\frac{\partial L_r}{\partial\varphi}\right)^2 + \left(\frac{1}{r}L_z\frac{\partial L_{z'}}{\partial\varphi} - \frac{1}{r}L_r L_\varphi + \frac{1}{r}L_r\frac{\partial L_r}{\partial\varphi}\right)^2 + \left(-\frac{1}{r}L_\varphi\frac{\partial L_{z'}}{\partial\varphi}\right)^2\right)$$

We now assume that, when encircling the disclination line, the director L rotates around the rotation vector R, while remaining perpendicular to R, with R making an angle β with the z' axis. In this case the variation of the director L as a function of φ, near the disclination is given by:

$$\bar{L} = \left(\cos\psi\cos\varphi\cos\beta + \sin\psi\sin\varphi\right)\bar{e}_r + \left(-\cos\psi\sin\varphi\cos\beta + \sin\psi\cos\varphi\right)\bar{e}_\varphi - \cos\psi\sin\beta\bar{e}_z$$

with ψ the variable azimuthal angle of L for rotation around R. In the case of a disclination line, the azimuthal angle ψ increases by π when φ increases from 0 to 2π for a full rotation around the disclination line, or dψ/dφ=1/2. The resulting expression for F has many terms, but integration over a circle with radius r around the disclination line, with φ going from 0 to 2π, simplifies to:

$$\int_0^{2\pi} F\cdot r d\varphi = \frac{\pi}{16r}\left(K_{11}\left(1+\cos^2\beta\right) + 2K_{22}\sin^2\beta + K_{33}\left(1+\cos^2\beta\right)\right)$$

Integration between an inner radius r_{min} and an outer radius r_{max} leads to the elastic energy per unit length of the disclination line:

$$F_{disclination} = \frac{\pi}{16}\left(K_{11}\left(1+\cos^2\beta\right) + 2K_{22}\sin^2\beta + K_{33}\left(1+\cos^2\beta\right)\right)\ln\frac{r_{max}}{r_{min}}$$

This approximation is an over-estimation, because the energy may further be reduced by allowing additional degrees of freedom in which the rotation of the director is not uniform when encircling the disclination line.

S2 Polarization microscopy images of a larger area with disclinations of different types

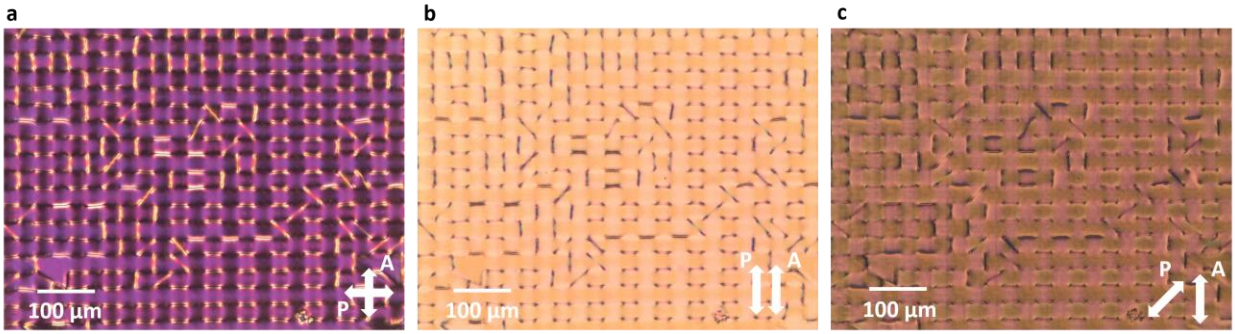

Figure S2. Polarization microscope images showing horizontal, vertical and diagonal disclination lines. **a** with crossed polarizers, **b** with parallel polarizers, **c** polarizers rotated over 45 degrees.